Powder Technology 338 (2018) 493–505

Contents lists available at ScienceDirect

Powder Technology

journal homepage: www.elsevier.com/locate/powtec

Dam-break of mixtures consisting of non-Newtonian liquids and granular particles

Xingyue Li, Jidong Zhao *

Department of Civil and Environmental Engineering, Hong Kong University of Science and Technology, Clearwater Bay, Kowloon, Hong Kong

ARTICLE INFO

Article history:
Received 17 April 2018
Received in revised form 10 June 2018
Accepted 5 July 2018
Available online xxxx

Keyword:
Coupled CFD-DEM
Dam break
Mixture
Non-Newtonian liquid
Granular particle
Solid-liquid interaction

ABSTRACT

This paper revisits the classical dam break problem based on coupled Computational Fluid Dynamics and Discrete Element Method (CFD-DEM) modeling and analysis. We consider the collapse of mixtures comprised of non-Newtonian liquids and particles, and compare them with cases of a particle-water mixture, a dry particle column and three pure liquids. In all cases, the fluid is simulated by the CFD, while the granular particles are modeled by the DEM. Interactions between the fluid and the particles are considered by exchanging interaction forces between the CFD and DEM computations. Both the macroscopic and microscopic characteristics of the particle system, the liquid and the mixture during the dam break are examined, with particular attention placed on the effect of solid-liquid interaction and the distinct flow behaviors considering non-Newtonian liquid in a mixture in comparison with water. The non-Newtonian liquids are found to conform with the particles well during the collapse process, in contrast to the separated profiles of water and particles. In comparison with pure liquid cases and dry particle case, the solid-liquid interactions are found to play a crucial role in affecting all aspects of the flow behavior of a mixture during its collapse, including the initiation of the collapse, the conformity of flow profile, the evolution of flow front and the energy change. The underpinning physical mechanisms are analyzed and correlated to the macro observations.

1. Introduction

Dam break refers to the collapse of an infinite or finite volume of fluid, particles or their mixture onto a horizontal or inclined channel. It represents a wide range of practical problems that are of great engineering importance [1]. The collapse of water-reserving dams or earth-filling tailings dams are among the most widely known examples. The failure of these dams may cause catastrophic damages to both human life and properties. For example, the overflow of reservoir water of Vajont dam in Italy caused by a landslide in 1963 killed 1910 people. More recently, the collapse of Situ Gintung water dam in Tangerang of Indonesia in 2009 claimed nearly 100 lives. Several recent devastating failures of mine/waste tailings dams have drawn global attentions on their threat to the environment and human life. One example is the collapse of Bento Rodrigues tailings dam occurring in Mariana, Brazil, on Nov. 5, 2015. The collapsed slurry wave flooded the town of Bento Rodrigues, killed at least 17 people and polluted several nearby rivers and over 15 km^2 of land [2]. A tailings dam of jade mine collapsed in northern Myanmar on Nov. 21, 2015 killed at least 113 people. Indeed, there have been over 40 similar major failures of tailings dams reported around the world since 2000 [3].

The scientific value of dam break has long been recognized, as an idealized problem for benchmark and verification for a range of theories and approaches in both mathematics and physics [4]. In as early as 1892, Ritter [5] has derived a theoretical solution for the flow front of water based on a simple dam break model. Late analytical studies have examined various aspects of dam break, including the effect of flow resistance [6, 7, 8, 9]. The majority of past studies on dam break considered the collapse of either pure fluids or dry particles, with only quite a few on particle-water mixtures [10, 11, 12, 13, 14, 15, 16, 17, 18, 19, 20]. The focus of the present study is placed on the collapsing of a mixture composed by granular particles and non-Newtonian fluids, in reference to engineering problems relevant to tailings dams or environmental flows such as volcanic lava, slurry and mud flows wherein the fluid involved is typically non-Newtonian [21]. Dam break of pure non-Newtonian fluids such as slurry and gel has been studied in [13, 14]. Other examples involving non-Newtonian fluids include the slump tests [22, 23, 24] on fresh concrete in civil engineering and Bostwick tests [25, 26, 27] for salad dressings in food industry. Consideration of non-Newtonian fluids indeed enables better explorations of more complex natural flows such as slurry than considering Newtonian fluids like water only.

Conventional continuum-based studies on dam break have commonly considered a particle-fluid mixture as an equivalent fluid or two fluids [28]. They have largely neglected the intricate interactions

* Corresponding author.
E-mail address: jzhao@ust.hk (J. Zhao).

https://doi.org/10.1016/j.powtec.2018.07.021
0032-5910/

between the fluid and the particle phases which could affect significantly the collapse behavior of the mixture. In this study, a coupled CFD-DEM approach [29, 30, 31, 32, 35, 36, 37] is employed to investigate the collapse of a mixture consisting of fluid and particles, where we will demonstrate that fluid-particle interactions within the mixture can be well captured. The CFD and DEM are used to model the fluid and particle phases in the mixture, respectively. The interactions between the fluid and particles are considered by exchanging fluid-particle interaction forces between the CFD and DEM computations. The coupled CFD-DEM simulations can capture both micro and macro flow characteristics during dam break, which could offer new insights into the microstructural origins underpinning macroscopic collapse and flow of a mixture.

2. Methodology, formulation and model setup

To simulate the dam break of a particle-fluid mixture, we employ the CFD [38] to solve the locally averaged Navier-Stokes equation for the fluid phase, and use the DEM [39, 40] to solve the Newton's equations governing the granular particles. Two open source software packages, namely, the OpenFOAM [41] and the LIGGGHTS [42], are adopted for the CFD and the DEM modules, respectively. The coupling between the CFD and the DEM is considered by exchanging interaction forces including drag force, buoyant force and viscous force. The coupling is implemented by a modified interface program based on the CFDEM originally developed by Goniva et al. [29] and later extended by Zhao and Shan [30]. Detailed solution procedures can be found in [30].

2.1. Governing equations for the particles and the fluid

The DEM [43] is employed to model the particle system in the mixture and to solve the following Newton's equations governing the translational and rotational motions of a particle i in the particle system

$$\begin{cases} m_i \dfrac{d\boldsymbol{U}_i^p}{dt} = \sum\limits_{j=1}^{n_i^c} \boldsymbol{F}_{ij}^c + \boldsymbol{F}_i^f + \boldsymbol{F}_i^g \\ I_i \dfrac{d\omega_i}{dt} = \sum\limits_{j=1}^{n_i^c} (\boldsymbol{M}_{t,ij} + \boldsymbol{M}_{r,ij}) \end{cases} \tag{1}$$

where m_i and I_i are the mass and moment of inertia of particle i, respectively. $\boldsymbol{U}_i^p$ and ω_i denote the translational and angular velocities of particle i, respectively. n_i^c is the number of total contacts for particle i. $\boldsymbol{F}_{ij}^c$ is the contact force acting on particle i by particle j or walls. $\boldsymbol{F}_i^f$ are the particle-fluid interaction forces acting on the particle. $\boldsymbol{F}_i^g$ is the gravitational force of particle i. $\boldsymbol{M}_{t,ij}$ and $\boldsymbol{M}_{r,ij}$ are the torques acting on particle i by the tangential force and the rolling friction force [44], respectively. The contact force $\boldsymbol{F}_{ij}^c$ is calculated as follows based on Hertzian-Mindlin contact law as illustrated in Fig. 1:

$$\boldsymbol{F}_{ij}^c = \left(k^n \delta_{ij}^{\boldsymbol{n}} - \gamma^n v_{ij}^{\boldsymbol{n}}\right) + \left[\left(\boldsymbol{F}_{spring}^{s0} + k^s \Delta\delta_{ij}^{\boldsymbol{t}}\right) - \gamma^s v_{ij}^{\boldsymbol{t}}\right] \tag{2}$$

where the terms on the right hand side refer to the normal spring force, the normal damping force, the shear spring force and the shear damping force, respectively. The total tangential force is the sum of shear spring force and shear damping force, denoted by the term in the square bracket. It increases until the shear spring force $\boldsymbol{F}_{spring}^s$ (i.e., $\boldsymbol{F}_{spring}^{s0} + k^s \Delta\delta_{ij}^{\boldsymbol{t}}$) reaches $\mu \boldsymbol{F}^n$, where μ is the friction coefficient and $\boldsymbol{F}^n$ is the total normal force in the first parenthesis. The tangential spring force is then held at $\boldsymbol{F}_{spring}^s = \mu \boldsymbol{F}^n$ during frictional sliding until the particles lose contact. $\boldsymbol{F}_{spring}^{s0}$ is the initial tangential spring force at the previous time step. k^n and k^s are the normal and tangential stiffnesses, respectively. $\delta_{ij}^{\boldsymbol{n}}$ is the overlap distance in the normal direction and $\Delta\delta_{ij}^{\boldsymbol{t}}$ is the incremental tangential displacement. γ^n and γ^s are the damping coefficients in the normal and tangential directions of the contact, respectively. $v_{ij}^{\boldsymbol{n}}$ and $v_{ij}^{\boldsymbol{t}}$ are the normal and tangential components of the relative velocity of the overlapped two particles.

The fluid phase in the mixture is considered to be continuous and is simulated with a discretized fluid domain in the CFD. The following continuity equation and the locally averaged Navier-Stokes equation are solved for each of the fluid cells

$$\begin{cases} \dfrac{\partial\left(\varepsilon_f \rho_f\right)}{\partial t} + \nabla \cdot \left(\varepsilon_f \rho_f \boldsymbol{U}^f\right) = 0 \\ \dfrac{\partial\left(\varepsilon_f \rho_f \boldsymbol{U}^f\right)}{\partial t} + \nabla \cdot \left(\varepsilon_f \rho_f \boldsymbol{U}^f \boldsymbol{U}^f\right) = -\nabla p - \boldsymbol{f}^p + \varepsilon_f \nabla \cdot \boldsymbol{\tau} + \varepsilon_f \rho_f \boldsymbol{g} \end{cases} \tag{3}$$

where ε_f denotes the void fraction (porosity). ρ_f is the averaged fluid density. $\boldsymbol{U}^f$ is the average velocity of the fluid in a CFD cell. p is the fluid pressure in the cell. $\boldsymbol{f}^p$ is the volumetric interaction force acting on the fluid by the particles within each cell. $\boldsymbol{\tau}$ is the viscous stress tensor. The fluid properties are assumed constant within each fluid cell.

We consider both Newtonian and non-Newtonian fluids in this study. The following constitutive equation is assumed to govern an incompressible, isothermal Newtonian fluid

$$\tau = \mu_f \dot{\gamma} \tag{4}$$

where μ_f is the fluid viscosity and $\dot{\gamma}$ is the shear rate. The Herschel-Bulkley model is considered for a non-Newtonian fluid [45, 46] as follows

$$\tau = \tau_c + \kappa \dot{\gamma}^n \tag{5}$$

where τ_c is the yield stress of fluid, κ is the consistency index and n is the flow index. The following constitutive equation is considered for a Bingham fluid

$$\tau = \tau_c + \mu_f \dot{\gamma} \tag{6}$$

It is evident that the Herschel-Bulkley model in Eq. (5) can recover a Bingham fluid in Eq. (6) when the flow index n is set to 1.

2.2. Fluid-particle interactions

The coupling between the particles and the fluid is considered through the exchange of interaction forces $\boldsymbol{F}_i^f$ in Eq. (1) and $\boldsymbol{f}^p$ in Eq. (3) between the DEM and CFD computations. The interaction force acting on a considered particle i from the fluid $\boldsymbol{F}_i^f$ is calculated by

$$\boldsymbol{F}_i^f = \boldsymbol{F}^b + \boldsymbol{F}^d + \boldsymbol{F}^v \tag{7}$$

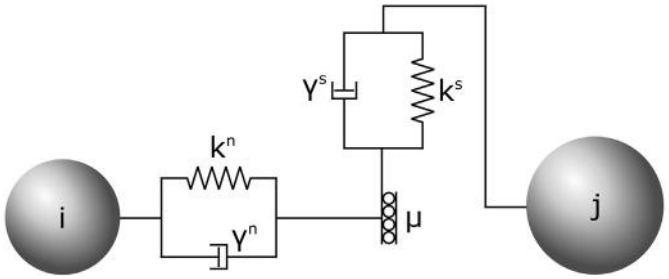

Fig. 1. Illustration of the Hertzian-Mindlin contact law used in the DEM simulation and the model parameters adopted (the normal and tangential stiffness: k^n and k^s; the damping coefficients for normal and tangential contacts: γ_n and γ_s; friction coefficient μ).

where $\boldsymbol{F}^b$, $\boldsymbol{F}^d$ and $\boldsymbol{F}^v$ are the buoyancy, the drag force and the viscous force, respectively. Other interaction forces such as virtual mass force, Basset force and lift force, which may be important in highly unsteady flow, are not considered in this study [47]. The volumetric fluid-particle interaction force for each fluid cell is

$$\boldsymbol{f}^p = \frac{1}{V_c}\sum_{i=1}^{n_c} \boldsymbol{F}_i^f \tag{8}$$

where V_c is the volume of a considered fluid cell. n_c is the number of particles in the fluid cell.

The buoyant force is defined as follows [48]

$$\boldsymbol{F}^b = \frac{1}{6}\pi\rho_f d_p^3 \boldsymbol{g} \tag{9}$$

where d_p is the diameter of the considered particle. The following expression is adopted for the drag force [49, 50]

$$\begin{cases} \boldsymbol{F}^d = \frac{1}{8}C_d\rho_f\pi d_p^2\left(\boldsymbol{U}^f - \boldsymbol{U}_i^p\right)\left|\boldsymbol{U}^f - \boldsymbol{U}_i^p\right|\varepsilon_f^{-\chi} \\ C_d = \left(0.63 + \frac{4.8}{\sqrt{Re_p}}\right)^2 \\ Re_p = \frac{\varepsilon_f\rho_f d_p\left|U^f - U^p\right|}{\mu_f} \\ \chi = 3.7 - 0.65\ \exp\left[-\frac{\left(1.5 - \log_{10}^{Re}p\right)^2}{2}\right] \end{cases} \tag{10}$$

where C_d is the drag coefficient depending on the particle Reynolds number Re_p, $\varepsilon_f^{-\chi}$ is a corrective function that accounts for the influence of other particles in the system on the drag force of the considered particle. The corrective function is related to both the porosity ε_f and the flow regime reflected by χ depending on the grain Reynolds number Re_p.

The viscous force induced by the fluid shear [51–53] is calculated by [54]

$$\boldsymbol{F}^v = -(\nabla\cdot\boldsymbol{\tau})V_i^p \tag{11}$$

where V_i^p is the volume of particle i.

2.3. Model setup for dam break simulation

Fig. 2 shows the model setup adopted for the subsequent numerical studies of dam break. The simulation domain is bounded by six boundary faces $F_1 - F_6$. A cubic sample (in blue in Fig. 2) with a dimension of $L \times H \times W$ is initially confined at the left side of a horizontal channel before the dam (in yellow in Fig. 2) is removed to release the sample for collapse. The dam is modeled as a rigid and removable wall in this study. In the DEM simulation, four channel boundaries F_1, F_2, F_5 and F_6 are assumed to form fixed, rigid and frictional walls for the particles. The right and upper faces F_3 and F_4 are assumed to be empty so that

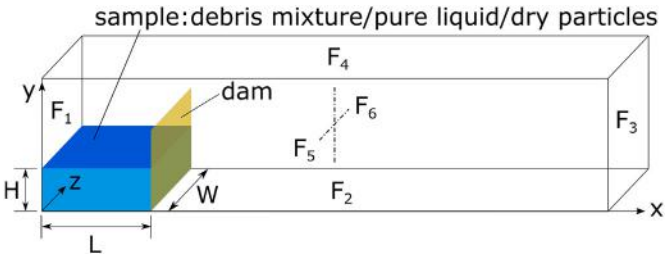

Fig. 2. Model setup of the dam break problem for CFD-DEM simulations (L: initial sample length, H: initial sample height, W: sample width).

any particles attempting to cross the right and upper boundaries can exit from the simulation. Correspondingly, the CFD domain is bounded by four no-slip boundary walls F_1, F_2, F_5 and F_6 (zero velocity and zero normal gradient for pressure), an outlet right face F_3 (zero velocity gradient and zero pressure gradient) and an atmosphere upper face F_4 (zero pressure) [55].

Table 1 summarizes a total of fourteen cases considered in this study. They can be categorized into two major groups. Group I simulations are aimed at verifying and calibrating the modeling of the non-Newtonian fluids and the particles to be used in Group II. The flow behaviors of mixtures consisting of different non-Newtonian fluids, with or without particles, are examined in Group II. Tables 2 and 3 summarize the adopted parameters of the fluids and the particles in the simulations. The time steps used in the DEM and the CFD are 5×10^{-7} s and 5×10^{-5} s, respectively. The determination of maximum time step for DEM is based on the criteria of the Reyleigh time [52], whilst the time step for CFD is determined referring to the typical coupling interval between CFD and DEM [31, 52]. Consequently, in this study, the CFD and DEM computations exchange information every 100 time steps of the DEM.

3. Benchmark and calibration

To verify the employed OpenFOAM and LIGGGHTS in simulating the dam break problem, seven cases (Group I in Table 1) are considered to examine the flow characteristics of two non-Newtonian fluids listed in Table 2 (i.e., the Herschel-Bulkley fluid and the Bingham fluid) and the granular material described in Table 3. The simulation results obtained by the OpenFOAM and LIGGGHTS are analyzed and compared against those obtained from both CFX simulations [15] and experiments [10, 11, 16, 56, 57].

3.1. Dam break of two non-Newtonian fluids

Fig. 3a depicts the scaled flow front evolution with the scaled time for the Herschel-Bulkley fluid by the OpenFOAM simulation, showing a good agreement with that by the commercial ANSYS CFX simulation from [15]. Note that the adopted properties of the Herschel-Bulkley fluid in our OpenFOAM simulation are identical with those in the CFX simulation in [15]. Our OpenFOAM predictions are also compared with experimental results. Fig. 3b shows a comparison of the scaled front evolution with the scaled time for the Bingham fluid by our OpenFOAM simulation results with the experimental data in [16] (adopting the same density ρ_f, consistency index κ and flow index n). X_f is the front position calculated from the position of dam $x = L$ in Fig. 2. t is time. T is

Table 1
Conducted CFDEM simulations of the dam break problem (a: aspect ratio).

	Case no.	Case name	Sample constituent(s)	Sample size			
				H(m)	L (m)	W (m)	$a = H/L$
Group I (Benchmark and calibration)	1	HB-I	Herschel-Bulkley fluid	0.13	0.5	0.32	0.26
	2	B-I	Bingham fluid	0.022	0.4	0.115	0.055
	3	P-I-I	Particles	0.55	0.9	0.6	0.611
	4	P-I-II	Particles	0.6	0.9	0.6	0.667
	5	P-I-III	Particles	0.65	0.9	0.6	0.722
	6	P-I-IV	Particles	0.7	0.9	0.6	0.778
	7	P-I-V	Particles	0.75	0.9	0.6	0.833
Group II (Dam break of mixtures in comparison with pure fluids and dry cases)	8	W	Water	0.6	0.9	0.6	0.667
	9	HB	Herschel-Bulkley fluid	0.6	0.9	0.6	0.667
	10	B	Bingham fluid	0.6	0.9	0.6	0.667
	11	P	Particles	0.6	0.9	0.6	0.667
	12	W&P	Water+Particles	0.6	0.9	0.6	0.667
	13	HB&P	Herschel-Bulkley fluid+Particles	0.6	0.9	0.6	0.667
	14	B&P	Bingham fluid +Particles	0.6	0.9	0.6	0.667

Table 2
Adopted properties for the fluids for our modeling.

Fluid properties	Herschel-Bulkley fluid	Bingham fluid	Water	Air
Density ρ_f (kg/m^3)	1000	1400	1000	1
Consistency index κ (Pa·s^n)	4.279	4	0.001	1.48×10^{-5}
Flow index n	0.479	1	1	1
Yield stress τ_c (Pa)	30.002	2.1	0	0

the normalizer for time used in [16], which is calculated by $T = (L/H)(\kappa L/\rho g H^2)^{1/n}$, where L and H are the initial sample length and sample height, respectively. As yield stress is not considered in [16], we calibrate a yield stress 2.1 Pa which fits the experimental results well. Run 2 in Fig. 3b is a repeated experimental test of Run 1 in [16]. The above comparisons confirm that the OpenFOAM could provide accurate predictions for both Herschel-Bulkley fluid and Bingham fluid.

An apparent curvature change is observed at $t/T = 1000$ in Fig. 3a and at $t/T = 0.2$ in Fig. 3b for the scaled front evolution of the Herschel-Bulkley fluid and the Bingham fluid, respectively. The reflection points indeed correspond to a transition of flow from an inertial-dominated regime to a viscous-dominated one [15, 58, 59]. Early inertial-dominated flow is driven by the gravity and is accelerated to certain velocity and shear rate until the viscous dissipation becomes the dominant mechanism for energy dissipation which slows down the flow. Note that the final fluid in either case shown in Fig. 3 has not become steady before running out of the simulated boundary, otherwise a steady state would be observed.

3.2. Dam break of dry granular assembly

LIGGGHTS is also used to explore the collapse of five dry granular columns with different aspect ratios. The sample height ranges from 0.55 m to 0.75 m, as summarized in Table 1 (Cases 3–7). The transient flow structure during the flowing process and the final flow geometry when the system becomes steady are examined and compared with experimental observations [10, 11, 56, 57].

3.2.1. Internal flow structure

Fig. 4 shows the collapsing process of a typical dry granular column (Case P-I-II). At relatively small sample aspect ratio, Fig. 4a and b show that the top right portion of the column (above the dashed line) is mobilized by gravity, whilst the left bottom part remains a static wedge. The upper moving particles are gradually slowed down as shown in Fig. 4c and d due to shear friction by the lower particles and ground surface. These flow characteristics agree well with the experimental observations by Lube et al. [10] on granular columns with an aspect ratio $a < 1.15$.

A typical profile of the internal velocity during the lateral spreading of the granular column is shown in Fig. 5 for a cross section along the flow depth direction y. It shows a linear decrease of normalized velocity from around 4 to 0.5 with the decreasing normalized depth for particles close to the free surface ($y/d_p \gtrsim 15$). In contrast, an exponential trend is

Table 3
Adopted properties for the particles in the modeling.

Particle properties	
Diameter (m)	0.024
Density (kg/m^3)	2500
Young's modulus (GPa)	70 (particle-particle contact)
Young's modulus (GPa)	700 (particle-wall contact)
Poisson's ratio	0.3
Restitution coefficient	0.7 (particle-particle contact)
Inter-particle friction coefficient	0.7
Particle-bottom friction coefficient	0.7
Rolling friction coefficient	0.1

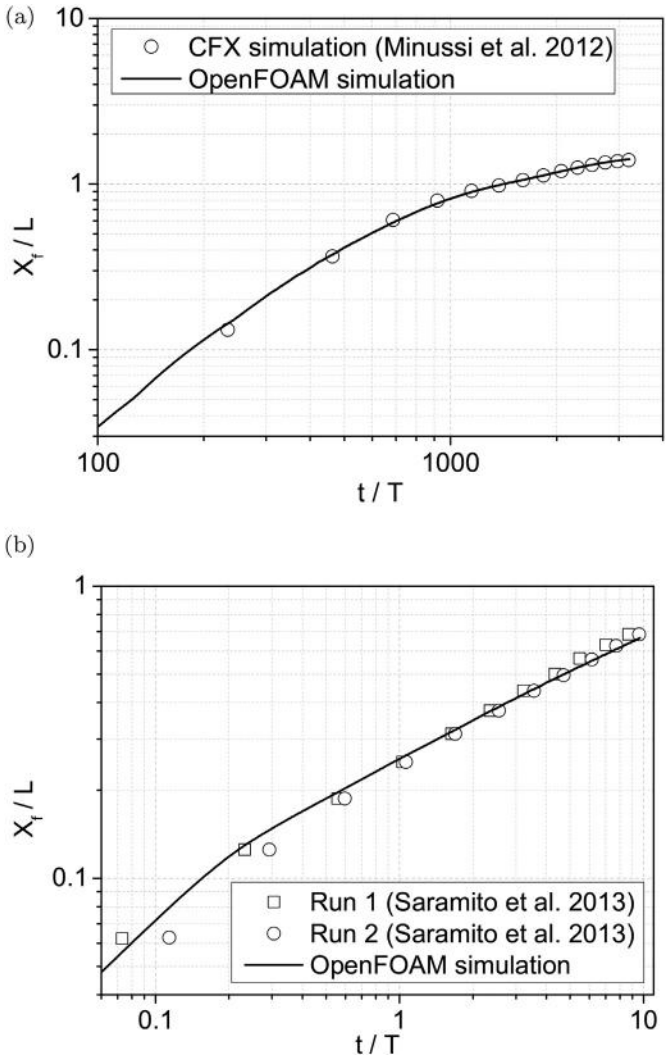

Fig. 3. Evolution of normalized front for (a) the Herschel-Bulkley fluid and (b) the Bingham fluid. The normalizers of time $T = (L/H)(\kappa L/\rho g H^2)^{1/n}$ are 4.374×10^{-4} s and 4.376 s for (a) the Herschel-Bulkley fluid and (b) the Bingham fluid, respectively.

observed for particles near the channel bottom (see $y/d_p \lesssim 15$ in the inset of Fig. 5). The change from an original linear velocity profile to an exponential profile from the free surface to the flow bottom coincides well with the experimental data obtained by Lajeunesse et al. [57] and Lube et al. [56], indicating a constant shear rate at the upper flow layer and a decreasing shear rate at the lower steady layer.

3.2.2. Final profile and runout at steady state

Interestingly, the scaled profiles of final deposition in the five cases almost overlap with each other as demonstrated in Fig. 6, where the final sample height h is scaled by the initial sample height H while the horizontal length $x - L$ is scaled by the final runout $l_\infty - L$ for each case. The runout is the traveled distance by a sample from $x = L$ to $x = l$, where l is the position of the flow front in the x coordinate in Fig. 2. The final runout is calculated as $l_\infty - L$ after the sample become steady, where l_∞ is the final front position measured from $x = 0$ in the coordinate showed in Fig. 2. The determination of final runout in our study has excluded particles detached from the main deposit. The universal scaled final profile in Fig. 6 has also been observed in experiments [11]. Note that our DEM modeling has considered particle rolling resistance (see [30–34]).

While the scaled deposition profile is independent of the aspect ratio of column, the normalized final runout (by the initial sample length) is indeed affected by the aspect ratio, according to the

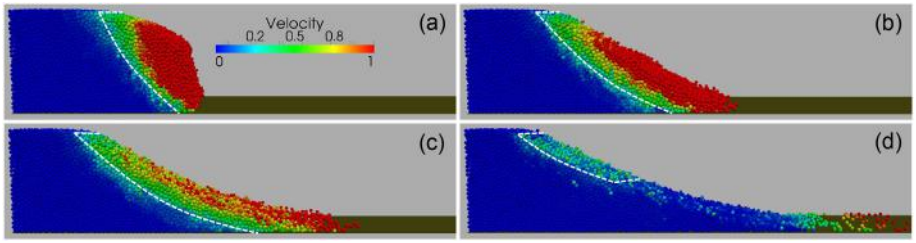

Fig. 4. Flow evolution with time in Case P-I-II (a) $t = 0.25$ s; (b) $t = 0.5$ s; (c) $t = 0.75$ s; (d) $t = 1.25$ s (The white dashed curves denote the fracture planes which separate stationary particles from moving particles).

following expression which was validated by the experimental data in [11]

$$\frac{l_\infty - L}{L} \sim \lambda(\delta, \phi) a^\alpha \tag{12}$$

where $l_\infty - L$ is the final runout distance calculated from the position of dam $x = L$, λ is a function of the bed friction angle δ and the internal friction angle ϕ, a is the aspect ratio and α is the power index. The function λ apparently varies with the friction coefficients. However, the power index α has been found to be a constant 0.9 ± 0.1 for a wide channel and 0.65 ± 0.05 for a narrow slot by experiments [11]. Fig. 7 depicts five data points from our dry column simulations. A power law correlation between the scaled final runout and the aspect ratio is found, with a power index $\alpha = 0.9884$. This agrees well with the range of 0.9 ± 0.1 in [11] for a wide channel.

4. Dam break of mixtures consisting of non-Newtonian fluids and particles

To explore the significance of solid-fluid interactions in a typical debris mixture and the distinct flow kinematics in consideration of viscous non-Newtonian fluids and water, the two non-Newtonian fluids and the dry granular material discussed in Part 3 have been employed to form the debris mixtures in Case HB&P and Case B&P in Table 1. We have also investigated five comparison cases, including a mixture case (Case W&P) where the sample is composed by water and the dry material, a dry case (Case P), and three pure fluid cases (Case W, Case HB and Case B). The initial samples in these seven cases possess an identical dimension ($H = 0.6$ m, $L = 0.9$ m, $W = 0.6$ m).

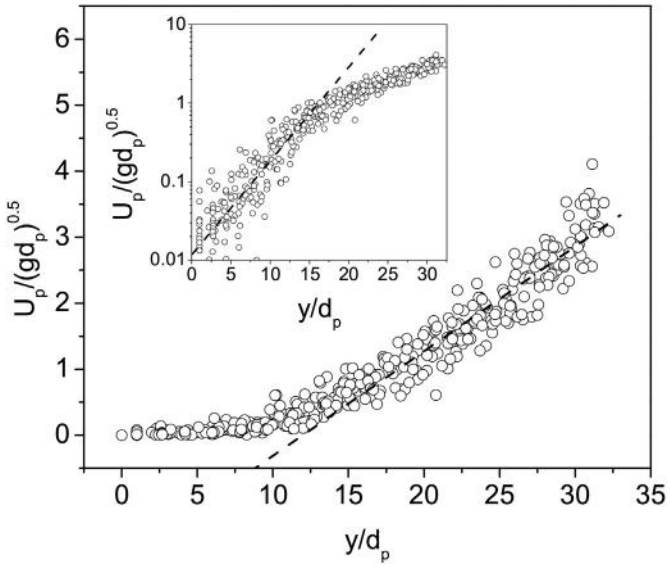

Fig. 5. Typical normalized velocity profile as a function of normalized depth (Case P-I-II, $t = 0.5$ s, $x = 0.8$ m). The inset shows the identical data in a linear-log scale to demonstrate the exponential relation for particles close to the channel bed, in comparison with the linear relation for particles near the free surface.

4.1. Profile evolution

Fig. 8 presents the profiles of the mixtures at $t = 0.63$ s after collapsing, showing notable differences due primarily to distinct liquid properties. The initial particle packing and boundary conditions are identical in three mixture cases. For Case W&P consisting of water and particles, the free surface of the granular system (dotted line) separates appreciably from that of the liquid (dashed line). The granular phase has a higher flow height near the left boundary wall and a smaller runout, indicating a weak mixing between the two phases. In contrast, both Case HB&P and Case B&P demonstrate rather consistently overlapped profiles (solid line) of the granular and liquid phases, showing a good mixing of the viscous non-Newtonian liquids with the particles.

The normalized flow profile of the mixture in Case HB&P is further compared with that of the corresponding pure liquid case (Case HB) and the dry case (Case P) in Fig. 9 and Fig. 10. The evolutions of normalized profile from $t = 0.5$ s to $t = 1.0$ s in the three cases are demonstrated in Fig. 9. The maximum flow height near the left boundary wall normalized with respect to the initial sample height decreases from 0.997 to 0.894 for the mixture in Case HB&P, and drops significantly from 0.811 to 0.465 for the liquid in Case HB. The normalized maximum flow height in the dry case (Case P) remains almost constant due to the presence of stationary wedge (dead zone) discussed in Part 3.2. The fronts of the three cases evolve in the following order in terms of front velocity: Case HB > Case HB&P > Case P. Moreover, the surface slope angle declines during the dam break before reaching the equilibrium state, wherein Case HB and Case P have the largest and smallest decreasing rate, respectively. These observed tendencies relate well to the solid-liquid interaction in the mixture case (Case HB&P).

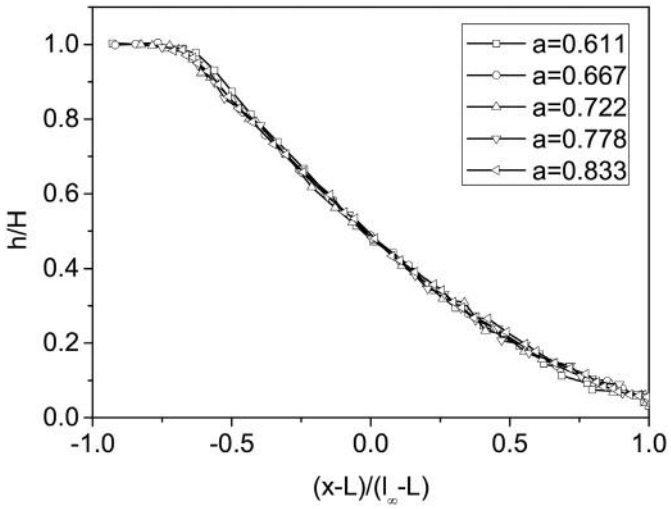

Fig. 6. Normalized final profiles under different aspect ratios.

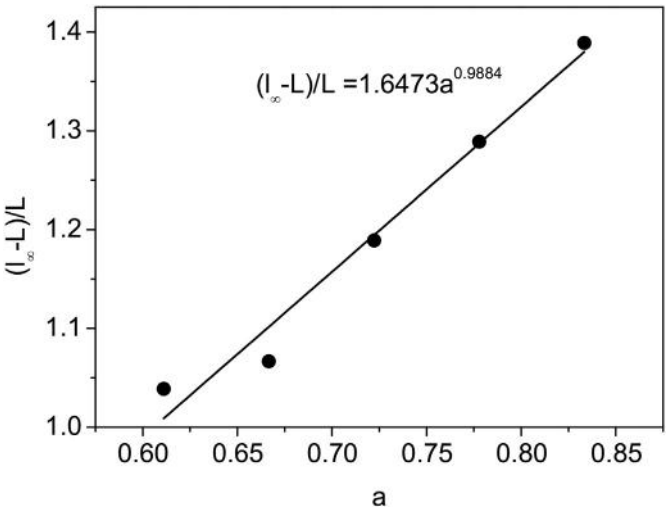

Fig. 7. Scaled final runout under different aspect ratios.

During the collapsing period ($t = 0.5 \sim 1.0$ s), the interaction forces acting on particles from the liquid in Case HB&P help to enhance the movement of the particles, which in turn slows down the motion of the liquid itself. Fig. 10 further shows the normalized profiles of the granular material in Case P, the liquid in Case HB and the mixture in Case HB&P at $t = 0.75$ s. Indeed, the intermediate profile of the mixture (as compared to pure fluid and dry particle cases) clearly reflects the interacting fluid/particles in the mixture and its enhancing effect on the granular system as well as retarding on the liquid phase. The relatively minor difference observed between Case HB&P and Case P in Fig. 10 shows a more dominant effect of the granular phase than the liquid, which might be due to the high volumetric concentration of the granular particles (60.56%) used in this study.

4.2. Front evolution

It is interesting to show the front evolutions of the liquid phase and the granular phase. The liquid fronts in the three pure liquid cases and

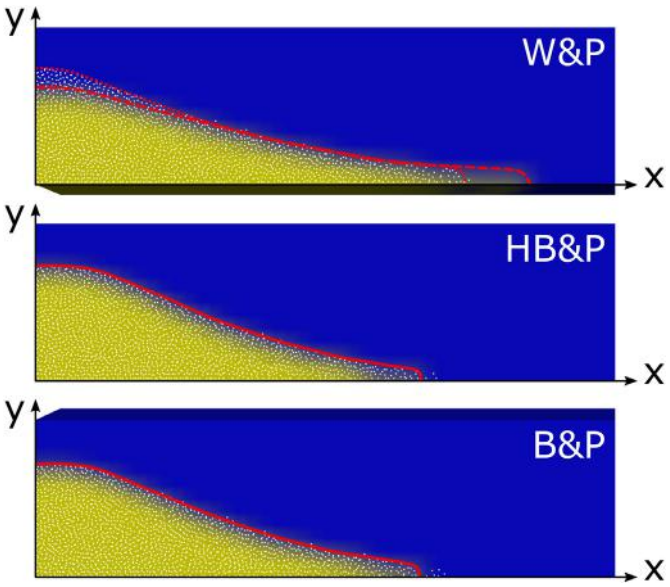

Fig. 8. Sample profiles at $t = 0.63$ s in three mixture cases (white dots denote the particle center; yellow and blue regions are liquid and air separately; W, HB, B and P denote water, Herschel-Bulkley fluid, Bingham fluid and particles, respectively). (For interpretation of the references to colour in this figure legend, the reader is referred to the web version of this article.)

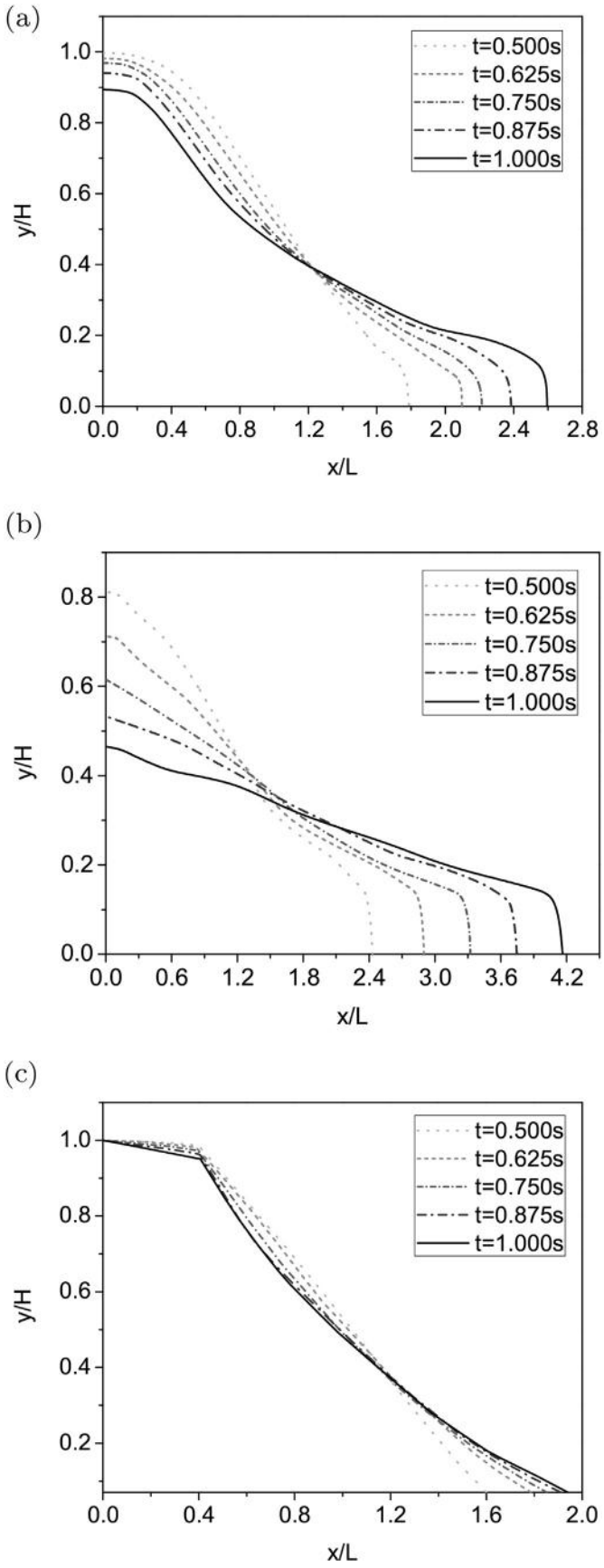

Fig. 9. Evolution of normalized sample profile from $t = 0.5$ s to $t = 1.0$ s (a) Case HB&P (b) Case HB (c) Case P.

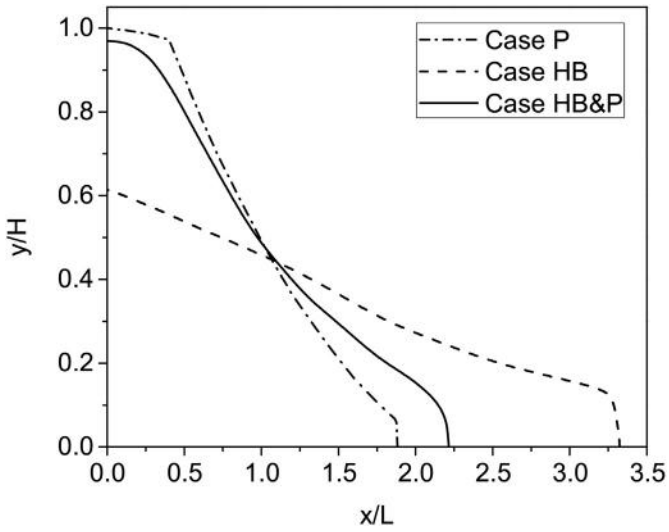

Fig. 10. Normalized sample profiles in Case HB&P, Case HB and Case P at $t = 0.75$ s.

the three mixture cases are firstly discussed to explore the effect of particles on the liquid front evolution. The fronts of granular particles in the dry case and the three mixture cases are then examined to study the influence of liquids. Fig. 11 shows the liquid front evolutions in the pure liquid cases and the mixture cases. For three pure liquid cases (Case W, Case HB and Case B, in blue), the liquid fronts initially coincide with one another from $t = 0$ s to $t = 0.3$ s, but later demonstrate appreciable deviations, with water in Case W going faster than the Herschel-Bulkley fluid in Case HB and the Bingham fluid in Case B. The smaller viscosity and zero yield stress of water as compared with the Herschel-Bulkely fluid and the Bingham fluid play an apparent role. Meanwhile, the faster fluid front in Case HB than in Case B is due to the shear thinning effect of the Herschel-Bulkley fluid ($n = 0.479 < 1$).

The presence of granular particles in the mixture cases notably changes the evolution of the liquid fronts, as shown in Fig. 11. Two stages of the liquid front evolution can be identified for three mixture cases. At Stage I $t = 0 \sim 2.3$ s, the front of water in Case W&P travels faster than the Bingham fluid in Case B&P, with the Herschel-Bulkley fluid in Case HB&P lagging the last. For Stage II from $t = 2.3 \sim 2.5$ s, the front of the Bingham fluid in Case B&P exceeds that of the water in Case W&P and becomes the fastest in the three mixture cases. While the Bingham fluid in Case B has the slowest front among three pure liquid cases, it surpasses the Herschel-Bulkley fluid in mixture case and further overtakes the water in Stage II due mainly to its larger density compared to the other two liquids in the mixture cases. At the early stage, the small effective viscosity of water leads to its fastest front, but the relatively high liquid density of the Bingham fluid later on provides larger dragging on the particles which results in its higher flow mobility and faster front. The change of front evolution in the mixture cases demonstrates the obvious effect of the particles and the significance of solid-fluid interactions, whereby the dominant mechanism in pure fluid cases by fluid effective viscosity may be weakened.

Apart from the liquid front, the front evolutions of the granular system in the three mixture cases and the dry case are also investigated. As shown in Fig. 12, at the early stage ($t = 0 \sim 0.25$ s), the front of particles in Case P does not show notable difference with that in Case HB&P and Case B&P, indicating the trivial effect of the non-Newtonian liquids. However, the faster fronts in mixture cases when $t > 0.25$ s clearly indicate the enhanced mobility of the granular system in comparison with the particles in the dry case (Case P). Similar to the liquid front of the mixture cases in Fig. 11, the granular front evolutions in the mixture cases can be characterized by two stages, whilst the dry particle front in Case P largely remains the slowest one in all stages compared to the other three mixture cases. For the three mixture cases, the particle front of Case W&P evolves faster than those in Case B&P and Case HB&P at Stage I, whilst the order changes to Case B&P > Case W&P > Case HB&P at Stage II. The transition boundary between these two stages for the granular front is found at $t = 0.95$ s, which is much earlier than that for the liquid front $t = 2.3$ s in Fig. 11. As further shown in Fig. 13, the magnitude of relative velocity between the fluid and particle phases in Case B&P is significantly smaller than that in Case W&P, reflecting a stronger driving effect of the Bingham liquid on the granular system than that of water in Case W&P.

4.3. Evolution of kinetic energy and energy change

It is instructive to analyze the energy transfer and dissipation of the mixtures during the dam break to investigate roles of solid-fluid interactions during the process. Fig. 14 shows the evolutions of the kinetic energy. Notably, the kinetic energy of the granular phase $E_{kp}^{CaseW\&P}$ appears to be smaller than that of the liquid system $E_{kf}^{CaseW\&P}$ in Case

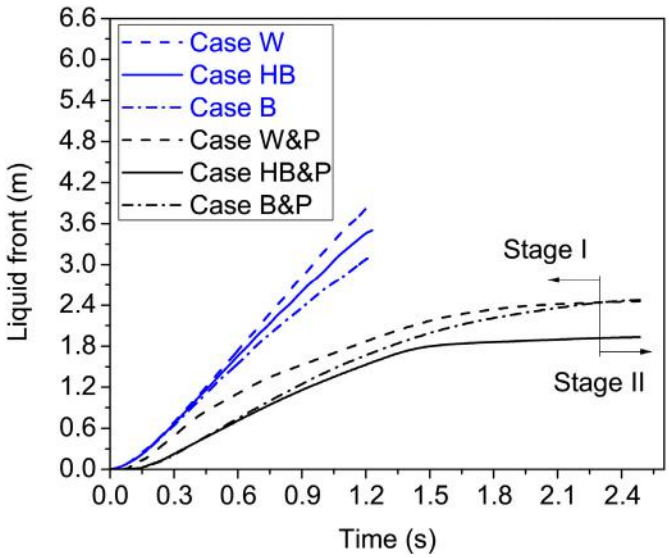

Fig. 11. Evolution of liquid front in three pure liquid cases and three mixture cases.

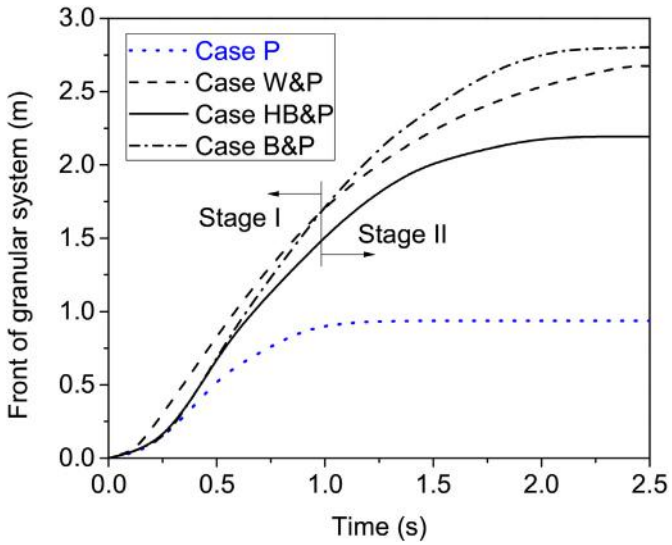

Fig. 12. Front evolution of the granular system in a dry case and three mixture cases.

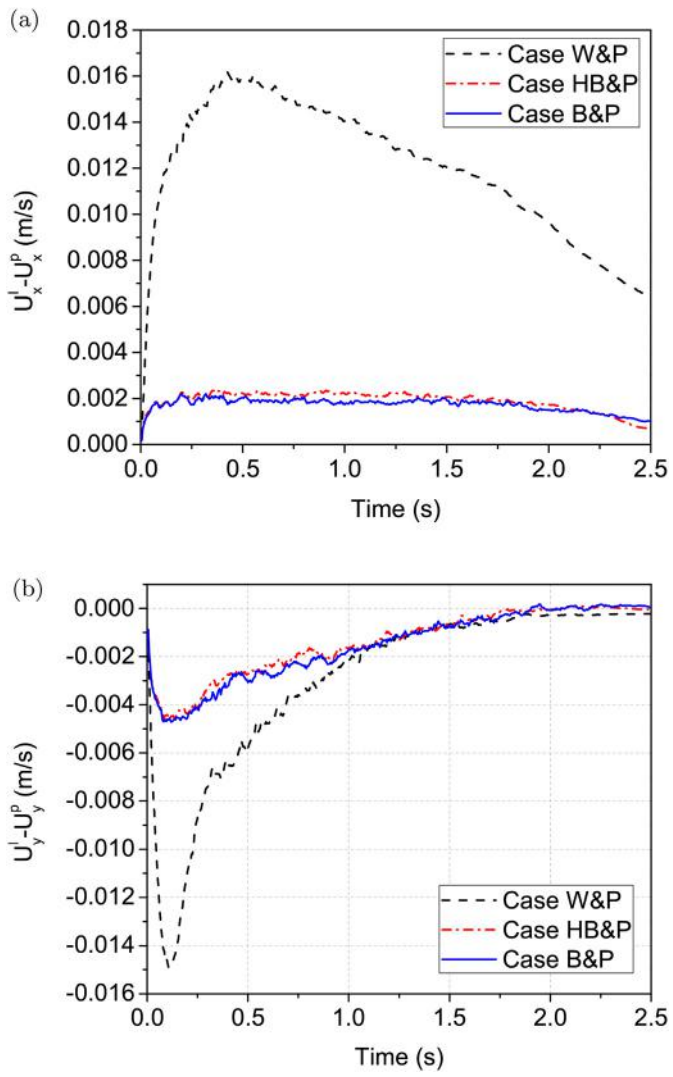

Fig. 13. Evolution of relative velocity between the liquid system and the granular system (U_x^l, U_x^p and U_y^l, U_y^p denote the average velocity of the liquid system and the particles along x and y directions).

W&P, whereas in both cases of HB&P and B&P, the granular system has a larger kinetic energy. Although the particle phase still has a smaller magnitude of average velocity than the liquid system, the relative velocity between the two phases in Case HB&P and Case B&P is not significant, as shown in Fig. 13, due to bigger drag and better mixing and consistency between the two phases with larger viscosity of the constituent two non-Newtonian liquids than water in Case W&P. Meanwhile, the high density and mass of the solid phase takes weight towards the overall kinetic energy, leading to a larger kinetic energy of the solid phase in Case HB&P and Case B&P. Note that the mild kink of E_{kf}^{CaseW} at around 1.25 s and $E_{kf}^{CaseW\&P}$ at 1.39 s in Fig. 14a and E_{kf}^{CaseHB} at around 1.38 s in Fig. 14b are caused by the loss of liquid when some of the liquid flows out the simulation domain.

It is also noticed that the mixture case always has a smaller liquid kinetic energy as compared to the corresponding pure liquid case. The retarding effect of the granular phase apparently plays a role in dragging down the liquid movement. However, the granular phase in mixture case does not necessarily have a larger kinetic energy than its corresponding dry case. Fig. 14a and b show $E_{kp}^{CaseP} > E_{kp}^{CaseHB\&P}$ and $E_{kp}^{CaseP} > E_{kp}^{CaseB_{\&P}}$ at the early stage of collapse ($t = 0 \sim 0.25$ s), indicating the impeded mobility of the granular system by the two non-Newtonian liquids as compared to water. This can be illuminated by the normalized energy dissipation difference of the particles E_d^p in the three mixture

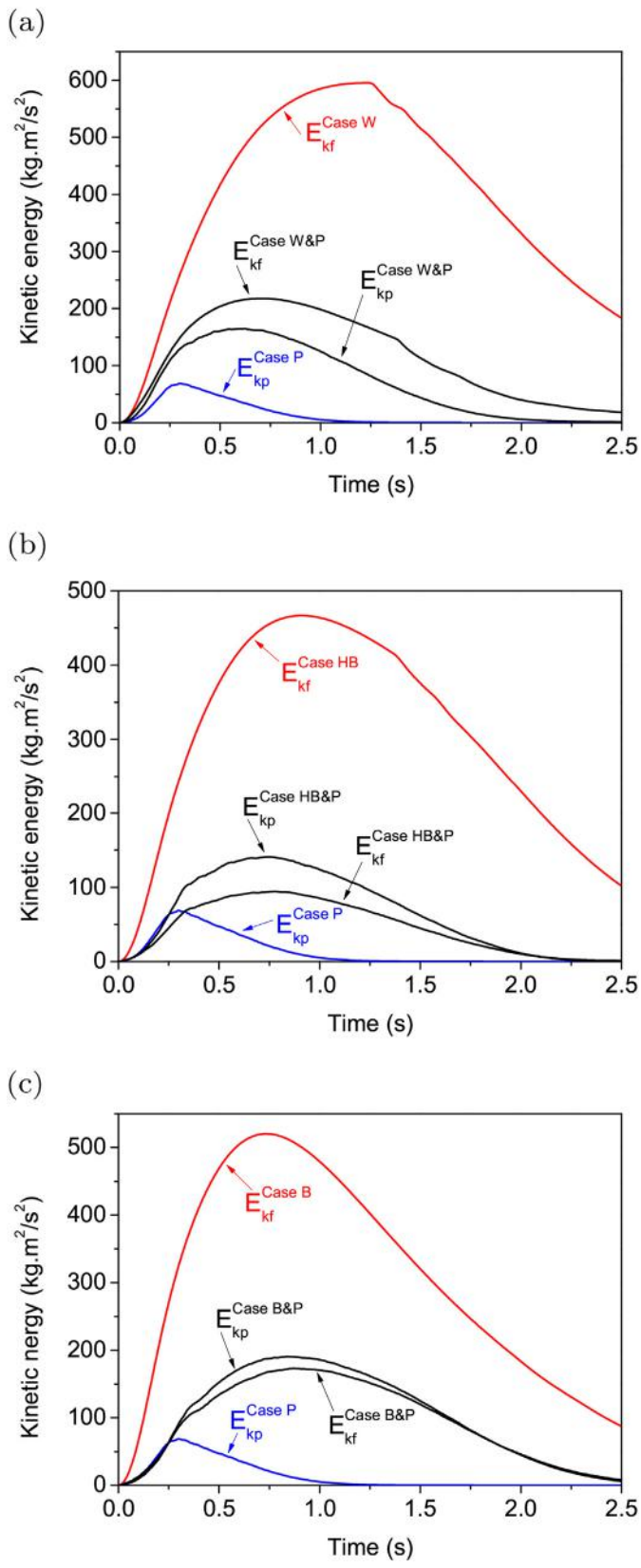

Fig. 14. Evolution of kinetic energy for the particles and liquid during the dam break. (a) Case P, Case W and Case W&P; (b) Case P, Case HB and Case HB&P; (c) Case P, Case B and Case B&P. In the figure, E_{kp} and E_{kf} represent the kinetic energy of the particles and the liquid, respectively.

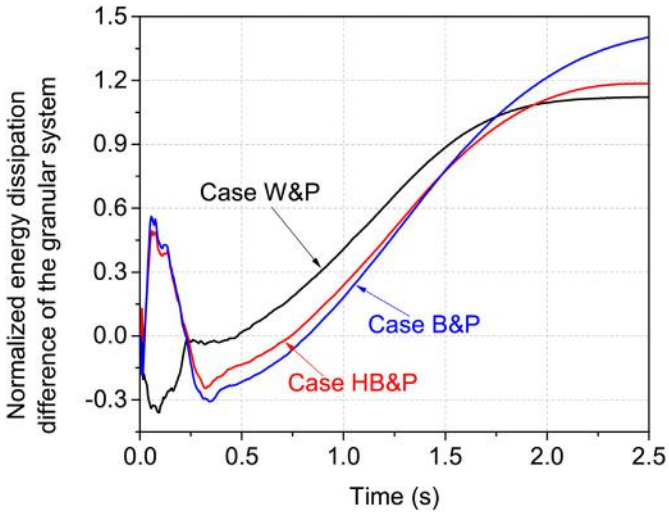

Fig. 15. Evolution of normalized energy dissipation difference of particles between the mixture case and the dry case.

cases relative to the dry case as shown in Fig. 15. The normalization is calculated by

$$E_d^p = \frac{\left[E_{pp}^{initial} - \left(E_{pp}^{current} + E_{kp}^{current}\right)\right]^{mixture} - \left[E_{pp}^{initial} - \left(E_{pp}^{current} + E_{kp}^{current}\right)\right]^{dry}}{\left[E_{pp}^{initial} - \left(E_{pp}^{current} + E_{kp}^{current}\right)\right]^{dry}} \tag{13}$$

where the numerator consists of two terms in the square brackets: the dissipated energy of the granular system in the mixture (in the first bracket) and the dissipated energy of the particles in the corresponding dry case (in the second bracket). The denominator is the dissipated particle energy in the dry case as well, serving as a normalizer. $E_{pp}^{initial}$ denotes the potential energy of the particles at the initial state before the mixture or the dry particle packing is released. $E_{pp}^{current}$ and $E_{kp}^{current}$ are the potential energy and kinetic energy of the particle system at the current time instant, respectively. Four sources were identified for energy dissipation for a dry granular system [32]: collisions between particles, collisions between particle and the channel boundary, friction between particles, friction between particle and the channel boundary.

The initial rise and peak in Fig. 15 for the three mixture cases are a result of small particle energy dissipation at the beginning of collapse in the dry case (as normalizer). The positive normalized energy dissipation difference in Case HB&P and Case B&P during $t = 0 \sim 0.25$ s signifies more dissipated energy of particles compared to the dry case, which reflects that energy is less effectively transferred from the liquid to the particles, resulting in a smaller kinetic energy of particles in the mixture cases (Case HB&P and Case B&P) during $t = 0 \sim 0.25$ s as shown in Fig. 14b and c $E_{kp}^{CaseHB\&P} < E_{kp}^{CaseP}$ and $E_{kp}^{CaseB\&P} < E_{kp}^{CaseP}$. In contrast, Case W&P has a negative normalized particle energy dissipation difference when $t = 0 \sim 0.25$ s, leading to $E_{kp}^{CaseW\&P} > E_{kp}^{CaseP}$ in Fig. 14a. These different effects of two non-Newtonian liquids and water at the initial stage of dam break are caused by the high viscosity of two non-Newtonian liquids and hint the more effective energy transfer from water to particles in Case W&P during this period. Nevertheless, when $t = 0.25 \sim 1.5$ s, the normalized particle energy dissipation difference in Case B&P becomes the smallest one, which indicates the most efficient energy transfer from the Bingham liquid to particles. As the mixture tends to stabilize after $t = 2.0$ s, Case W&P regains the least energy dissipation because of the large particle potential energy compared with Case HB&P and Case B&P.

The normalized energy dissipation difference of the granular system in Fig. 15 shows distinct effects of the non-Newtonian liquids and water on the particles during the collapse process. In turn, the energy dissipation of the liquid phase is affected by the particles as well. Fig. 16 shows the normalized overall energy change of the liquid phase E_c^f, calculated by the difference between the initial liquid potential energy $E_{pf}^{initial}$ and the sum of current potential and kinetic energies of the liquid (i.e., $E_{pf}^{current} + E_{kf}^{current}$), normalized by the initial liquid potential energy $E_{pf}^{initial}$ as follows

$$E_c^f = \frac{E_{pf}^{initial} - \left(E_{pf}^{current} + E_{kf}^{current}\right)}{E_{pf}^{initial}} \tag{14}$$

For pure liquid cases, the change indeed represents the energy dissipation during the collapse process. For the mixture cases, however, this energy change includes three parts: (1) the energy dissipation within the liquid phase (and with the boundaries), (2) the energy dissipated during particle-liquid interactions, and (3) the energy conservatively transferred to the particle phase through particle-liquid interactions. For the the pure liquid cases, it is depicted in Fig. 16 that the Bingham fluid in Case B has the largest cumulative energy dissipation, with the Herschel-Bulkley fluid in Case HB being the medium and the pure water case the smallest. The difference is attributable to the different flow resistances in the three liquids [60, 61]. The flow resistance may be influenced by many factors [62, 63], such as the channel cross-section shape, the boundary non-uniformity, flow unsteadiness, wall roughness and fluid viscosity. In this study, since the channels and boundaries for all cases are identical, the crucial factor is the fluid viscosity. As water has a smaller viscosity compared to the two non-Newtonian fluids, the energy dissipation induced in water is the smallest among all. The difference between the two non-Newtonian fluids depends on the shear-thinning or shear-thickening nature. The adopted Herschel-Bulkley fluid is a shearing-thinning one with a decreased viscous resistance in high shear rate regime. Not surprisingly, it shows a smaller energy dissipation as compared to the Bingham fluid. In the mixture cases, the water in Case W&P presents higher energy change than the other two non-Newtonian fluids. The Herschel-Bulkley fluid in Case HB&P is in the middle and the Bingham fluid in Case B&P is the smallest in most part. With small viscosity, the majority part of the energy change in the water phase is transferred to the particles to increase their kinetic energy, rather than being dissipated. This results in large overall velocities for both the particles and water in Case W&P, faster front evolution and quicker drawdown of potential. The rather conforming flow of particles with the non-Newtonian fluid in either cases of Case HB&P or Case

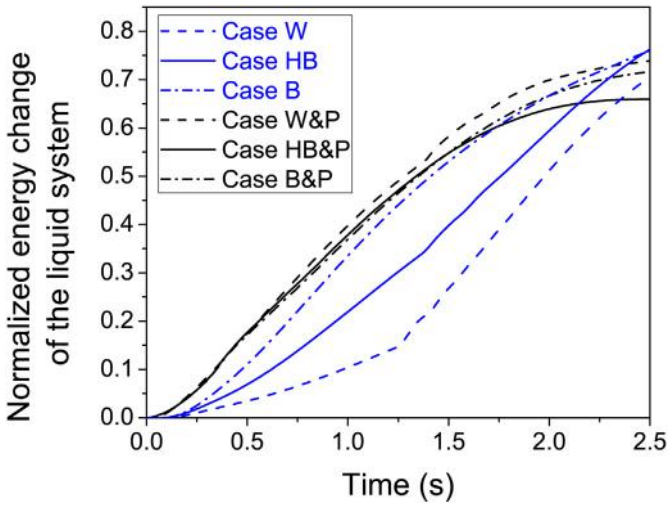

Fig. 16. Evolution of overall energy change of the liquid phase normalized by its initial potential energy in three pure liquid cases (Case W, Case HB and Case B) and three mixture cases (Case W&P, Case HB&P and Case B&P).

B&P during the collapse process leads to slow velocity changes for both phases and less overall energy changes than that in Case W&P.

4.4. Solid-liquid interactions

The preceding sections have shown compelling evidence on the influence of solid-fluid interactions on the flow profile, the front and the energy transfer and dissipation during the collapse of a mixture. Further discussion is devoted in this subsection to the correlation of solid-liquid interactions with the overall flow behavior. The total interaction force on the liquid phase by the particles during the flow has been calculated and further projected onto the flow direction x and the flow depth direction y. The results are shown in Fig. 17. In the horizontal direction, all three mixture cases show negative interaction forces imposed from the particles on the liquid (Fig. 17a), indicating the horizontal movement of the liquid mobilized by gravity is faster than that for the particles. This indeed is confirmed by the horizontal velocity difference presented in Fig. 13a. During the entire collapse process, the liquid imposes driving forces on the particles in the horizontal direction. Among the three cases, though the velocity difference in the water case is the largest, the magnitude of the interaction forces is the smallest due to the small viscosity of water compared to the other two non-Newtonian fluids.

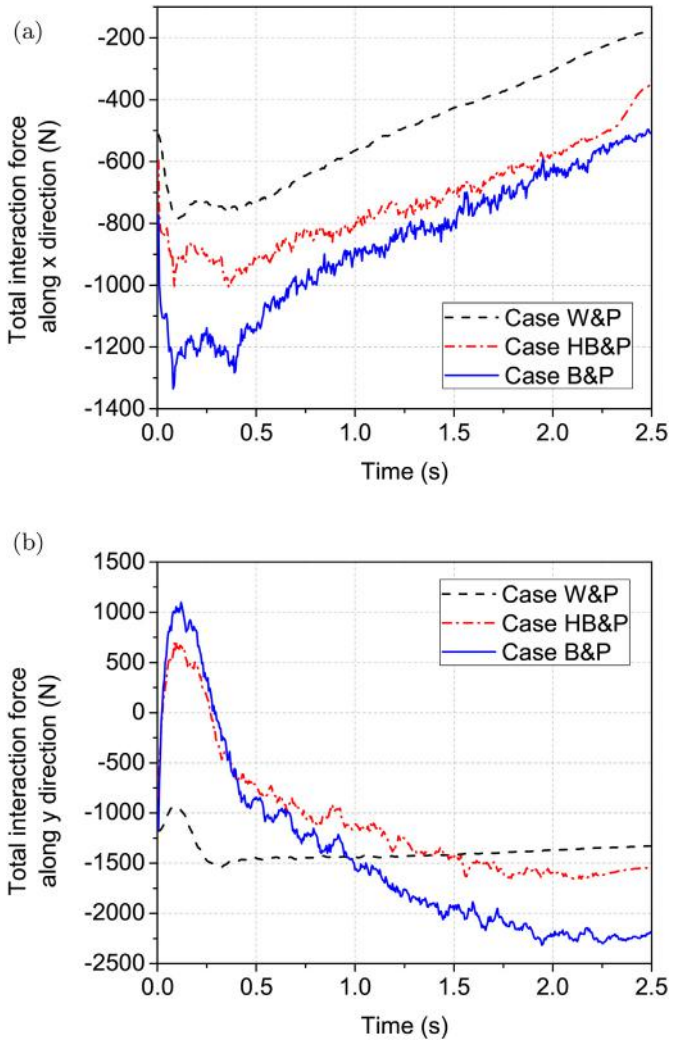

Fig. 17. Total interaction force acting on the liquid phase from the granular system along x (a) and y (b) directions.

Consistent observations can be found for the vertical direction from Fig. 17b. The negative vertical interaction forces at $t = 0$ s for all three cases are due apparently to the positive buoyant forces on the particles by the liquids before collapse. Once the dam is removed to allow the mixture to flow, Fig.13b shows that the gravity drives the liquid faster than it does on the particles, resulting in negative relative velocity between the liquid and the particles (note that upward velocity is positive) during almost all collapse stages for all three mixtures and extra upward drag force applied to the liquid. This gives rise to a quick increase of vertical interaction force to a peak at around $t = 0.125$ s for all cases in Fig. 17b. Again, the water case presents the largest magnitude of relative velocity among the three, but the drag force in the two non-Newtonian fluid cases is evidently much bigger than that in the water case due to bigger viscosity, leading to the change of vertical interaction forces from the initial negative to subsequent positive in cases HB&P and B&P while the force in Case W&P remains negative. The post-peak drop of vertical interaction forces in all three cases is due to the reduced magnitude of relative velocity after $t = 0.125$ s as shown in Fig. 13b.

The interaction forces shown in Fig. 17 not only help to clarify the flow behaviors of the liquid system, but shed light on the different behaviors of the granular phase when mixed with different liquids. It has been discussed in Fig. 14a that water always enhances the motion of the particles from their higher kinetic energy in comparison with dry particles. Indeed, the positive interaction force along x direction on the particles by the water drags the particles to the downstream side. In addition, the positive upward force along y direction by the water effectively reduces the frictional force of the particles, which from another aspect improves their mobility. However, in the two mixture cases involving non-Newtonian fluids, Fig. 14b and c indicate their kinetic energy of the particles is slightly smaller than that in the dry particle case before $t = 0.25$ s. Indeed, the time instant of $t = 0.25$ s coincides with that the total vertical interaction forces imposed to the liquids changing from positive to negative, as shown in Fig. 17b. At the early stage of collapse ($0\text{ s} < t < 0.25$ s), the non-Newtonian liquids drag the particles downwards, increasing the particle frictional force and inhibiting the motion of the particles. After $t > 0.25$ s, the two non-Newtonian fluids start to enhance the overall motion and kinetics of the particles as the water does.

4.5. Flow regimes

Froude number and Savage number are commonly used to examine the flow regimes for the liquid and granular particles, respectively. Froude number was originally proposed [64] to study the flow regime of fluid and has later been widely employed to dry granular system [65] and mixture [66]. It is defined by the ratio between the flow inertia and the external field (i.e., gravity field here) as follows

$$Fr = \frac{v}{\sqrt{gh}} \tag{15}$$

It is interesting to identify the effect of the particle phase on the flow regime of the liquid, and the Froude number of the liquid phase is focused on. v and h in Eq. (15) are the liquid velocity and depth, respectively. The flow corresponds to a subcritical, a critical and a supercritical flow when the Froude number is smaller than, equal to and larger than one, respectively.

Fig. 18 illustrates the evolution of Froude number of the liquid system in all six cases, where t and t_0 are the current time instant and the moment at which the liquid system arrives at the studied cross section $x = 1.38$ m. The moment that the liquid front arrives corresponds to the highest Froude number for the liquid. For the three pure liquids in Fig. 18a, their Froude numbers all decrease with time and follow the following relative order of magnitude at the same time instant: Water in Case W > Herschel-Bulkley liquid in Case HB > Bingham liquid in Case B. The

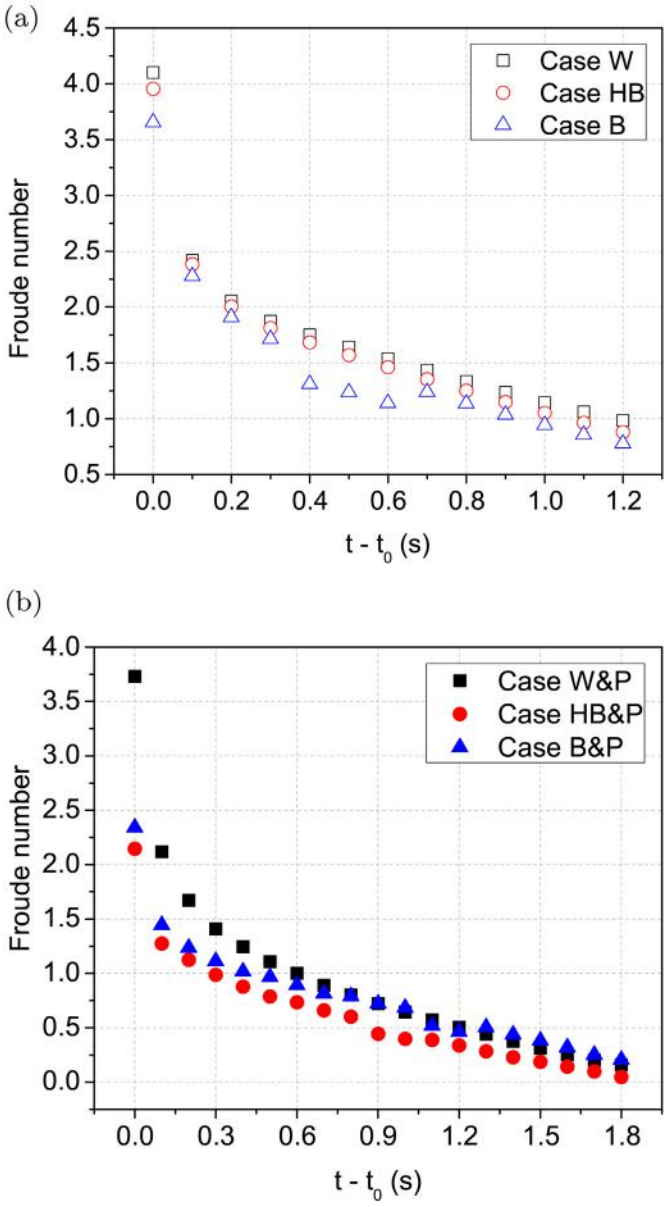

Fig. 18. Froude number of the liquid at $x = 1.38$ m in three pure liquid cases (a) and three mixture cases (b).

order is also consistent with the evolution of the liquid front (see Fig. 11) and the energy dissipation (see Fig. 16), where the liquid viscosity is the dominant mechanism for flow. Their Froude numbers indicate they are all supercritical flows when $t - t_0 < 1.0$ s. The Bingham fluid case experiences the earliest transition from supercritical to subcritical flow regime at $t - t_0 = 1.0$ s, with Case HB and Case W lagging slightly at $t - t_0 = 1.1$ s and $t - t_0 = 1.2$ s, respectively. Different observations are found in the mixture cases. Though the Froude number of the liquid in each of the three mixture cases also decreases with time, as shown in Fig. 18b, smaller Froude number is found than its corresponding pure liquid case at the same time instant, due apparently to the dragging effect by the particles. The transition time from a supercritical flow to a subcritical flow is shifted to earlier time instant, at $t - t_0 = 0.3$ s, 0.5 s and 0.6 s, respectively, for cases HB&P, B&P and W&P. The presence of particles apparently changes the relative magnitude of Froude number of liquid for Case HB&P and Case B&P. During the flow process, the Bingham liquid in Case B&P shows slightly higher Froude number than the Herschel-Bulkley liquid in Case HB&P. Water in Case W&P processes higher Froude number than the other two cases before $t - t_0 = 1.2$ s, but is overtaken by the Bingham liquid in Case B&P afterwards.

Savage number has been widely employed to characterize different flow regimes: friction dominant regime with a Savage number smaller than 0.1 and collision dominant regime otherwise. It is defined according to the ratio between the particle collision stress and particle friction stress [67, 68] as follows

$$N_{sav} = \frac{d_p \cdot \rho_s}{g \tan\phi} \cdot \frac{\dot{\gamma}^2}{\rho_s - \rho_f} \tag{16}$$

where d_p and ρ_s are the diameter and density of the particle. $\dot{\gamma}$ is the shear rate calculated by the velocity gradient along flow height direction at the top layer of the granular flow. ϕ is the internal friction angle. In our study, the initial granular packings in Case P, Case W&P, Case HB&P and Case B&P are identical and only the fluid density ρ_f and shear rate $\dot{\gamma}$ are varied in Eq. (16). The expression indicates that a higher shear rate and a higher fluid density give a larger Savage number and a more dominant role played by particle collisions. From a physical perspective, a higher shear rate or a larger velocity gradient hints more short-duration contacts or more collisions between particle layers, and a higher fluid density indicates a larger buoyancy and less friction between particles. Both mechanisms may lead to stronger particle collisions and a larger Savage number.

Fig. 19 presents the Savage number and the shear rate of the granular system at a selected cross section $x = 0.8$ m for four study cases. All four cases show an overall increasing-peak-decreasing trend, corresponding to an accelerating followed by decelerating processes of the granular phase during the dam break. The Savage number is generally found to be in the following order: Case B&P > Case P ≈ Case HB&P > Case W&P. Similar Savage numbers are found for Case P and Case HB&P, indicating a relatively minor influence of the Herschel-Bulkley liquid on the flow regime of the granular phase. This is indeed a combined effect of reduced shear rate (see Fig. 19b) and increased fluid density with the presence of the Herschel-Bulkley liquid. In contrast, the Bingham liquid and water considerably change the Savage number of the granular system, however in different ways. The presence of water decreases the shear rate and reduces the Savage number of the granular system, which is consistent with the observation in a previous study by Shan and Zhao [32]. Indeed, as shown in Fig. 20, the slope of velocity distribution at the top layer ($h \approx 0.31$ m) in Case W&P is gentle relative to that in the dry case ($h \approx 0.34$ m in Case P), rendering the granular system in Case W&P in a friction-dominated regime. The Bingham liquid in Case B&P leads to a larger shear rate than Case P and hence a larger Savage number. Moreover, the high density of the Bingham liquid provides greater dragging for particles, contributing an additional factor on the increase of Savage number. The overall granular system in Case B&P is thus collision-dominated from $t \approx 0.28$ s to $t \approx 1.1$ s.

5. Conclusions

The dam break problem for a mixture of particles and liquid has been numerically examined by a coupled CFD-DEM approach. The CFD was benchmarked on modeling of two non-Newtonian liquids against both commercial software and experimental data. The DEM was verified on modeling a granular system in comparison with experimental observations. The two calibrated numerical tools were then coupled to simulate the collapse of mixtures consisting of non-Newtonian liquids and granular particles. The simulation results were compared extensively against several control cases, including a mixture of water and particles, a dry granular system as well as three pure liquids (the Herschel-Bulkley liquid, the Bingham liquid and water). The unique flow characteristics of mixtures as compared to the single phase cases were examined, and their underlying physical mechanisms originated from the intricate solid-liquid interactions were identified. We capitalized the predictive power of the coupled CFD-DEM computational tool to capture the

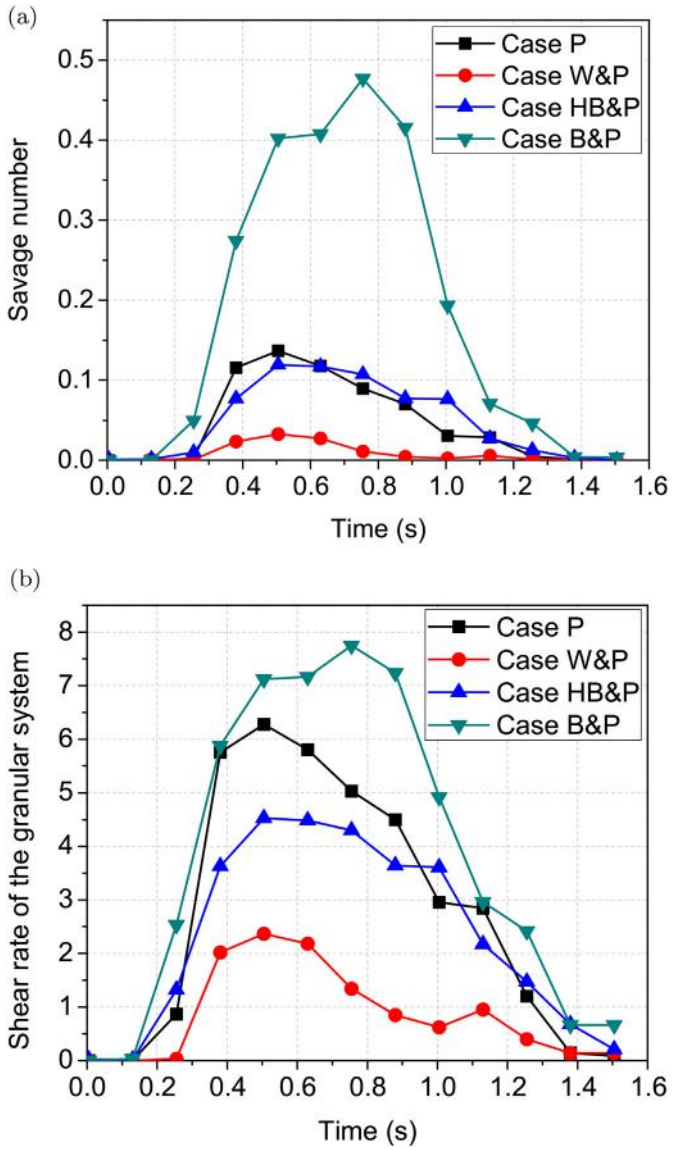

Fig. 19. Evolution of Savage number (a) and shear rate (b) for the cross section located at $x = 0.8$ m.

solid-liquid interactions in modeling the dam break problem and demonstrated that a single-phase continuum approach based on depth average is inadequate to describe the entire collapsing process of a mixture. Not only the viscous property but also the density of the liquid phase relative to the particles play a crucial role in early collapse and late developing stages of the dam break of a mixture. Indeed, the buoyancy in the solid-liquid interactions has been found important in late steady stage of the mixture flow, an observation consistent with the analysis in [28]. Major conclusions drawn from the study are summarized in the following:

- High effective viscosity of non-Newtonian liquids helps them better mix with granular particles during the flow as compared to water. The overall flow profile of the viscous non-Newtonian liquid shows good conformity with that of the mixed granular phase during the collapse of the mixture.
- Moving fronts of solid and liquid phases in a mixture are significantly affected by solid-liquid interactions. The dominant effect of fluid viscosity which controls front evolution of a pure liquid can be debilitated for the front evolution of an identical liquid mixed with particles.
- The change of kinetic energy of particles during the collapse reflects the distinct effects of non-Newtonian liquids and water. In contrast to the improved motion of particles by water throughout the dam break, the non-Newtonian liquids may reduce the particle kinetic energy at the early collapse before the subsequent enhancement effect.
- The solid-liquid interaction force underpins well the changed macro flow behaviors (i.e., flow front and flow energy) of the liquid and the particles in a mixture in comparison with the corresponding pure liquid and dry particles.
- With consideration of solid-liquid interaction for the liquid and the particles in a mixture, the liquid system initially characterized as a supercritical flow in a pure liquid case may be transformed into a subcritical one in a mixture case. Meanwhile, the flow regime of the granular packing in a dry case can be shifted to a collision-dominated or friction-dominated regime with the appearance of different liquids.

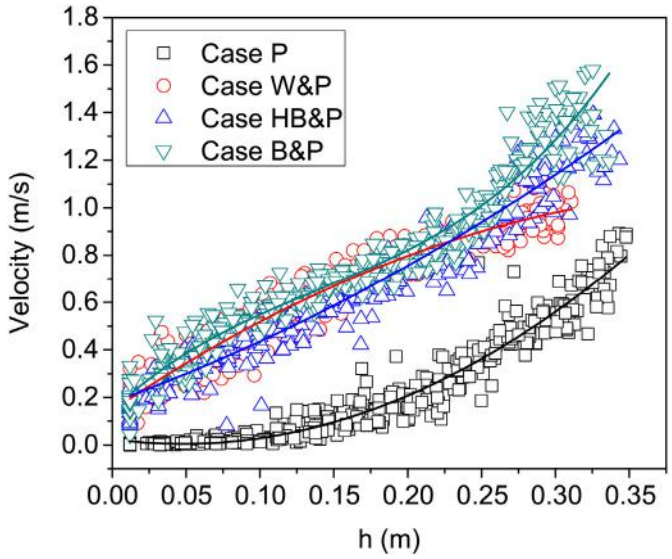

Fig. 20. Velocity distribution along height at $x = 0.8$ m and $t = 0.755$ s.

Acknowledgements

The research reported in this study was financially supported by the University Grants Council of Hong Kong by a Theme-based Research Scheme (TBRS) project T22–603/15 N, a Collaborative Research Fund (CRF) project C6012-15G and a RGC/GRF project 16205418. The first author acknowledges the financial support of Hong Kong PhD Fellowship on her PhD study.

References

[1] H. Chanson, Tsunami surges on dry coastal plains: application of dam break wave equations, Coast. Eng. J. 48 (4) (2006) 355–370.
[2] http://fundaoinvestigation.com/.
[3] http://www.wise-uranium.org/mdaf.html.
[4] J.S. Wang, H.G. Ni, Y.S. He, Finite-difference TVD scheme for computation of dam-break problems, J. Hydraul. Eng. 126 (4) (2000) 253–262.
[5] A. Ritter, Die fortpflanzung der wasserwellen, Zeitschrift des Vereines Deutscher Ingenieure 36 (33) (1892) 947–954.
[6] R.F. Dressler, Hydraulic resistance effect upon the dam-break functions, Natl. Bur. Stand. 49 (3) (1952) 217–225.
[7] G. Whitham, The effects of hydraulic resistance in the dam-break problem, Proc. R. Soc. Lond. 227 (1170) (1955) 399–407.
[8] B. Hunt, Asymptotic solution for dam-break problem, J. Hydraul. Div. 108 (1) (1982) 115–126.
[29] H. Chanson, Applications of the Saint-Venant equations and method of characteristics to the dam break wave problem, Technical Report CH55-05, Department of Civil Engineering, The University of Queensland, Brisbane, Australia, May 2005.
[10] G. Lube, H.E. Huppert, R.S.J. Sparks, A. Freundt, Collapses of two-dimensional granular columns, Phys. Rev. E 72 (4) (2005), 041301. .
[11] N. Balmforth, R. Kerswell, Granular collapse in two dimensions, J. Fluid Mech. 538 (2005) 399–428.

[12] C. Di Cristo, A. Leopardi, M. Greco, Modeling dam break granular flow, Proceedings of International Conference of River Flow 2010, pp. 895–901.
[13] C. Ancey, S. Cochard, The dam-break problem for Herschel-Bulkley viscoplastic fluids down steep flumes, J. Non-Newtonian Fluid Mech. 158 (1–3) (2009) 18–35.
[14] G. Chambon, A. Ghemmour, D. Laigle, Gravity-driven surges of a viscoplastic fluid: an experimental study, J. Non-Newtonian Fluid Mech. 158 (1–3) (2009) 54–62.
[15] R.B. Minussi, G.d.F. Maciel, Numerical experimental comparison of dam break flows with non-Newtonian fluids, J. Braz. Soc. Mech. Sci. Eng. 34 (2) (2012) 167–178.
[16] P. Saramito, C. Smutek, B. Cordonnier, Numerical modeling of shallow non-Newtonian flows: part I. The 1D horizontal dam break problem revisited, Int. J. Numer. Anal. Model. Ser. B 4 (3) (2013) 283–298.
[17] T. Ward, C. Wey, R. Glidden, A. Hosoi, A. Bertozzi, Experimental study of gravitation effects in the flow of a particle-laden thin film on an inclined plane, Phys. Fluids 21 (8) (2009), 083305. .
[18] N. Andreini, Dam Break of Newtonian Fluids and Granular Suspensions: Internal Dynamics MeasurementsPh.D. thesis École Polytechnique Fédérale de Lausanne, 2012.
[19] C. Ancey, N. Andreini, G. Epely-Chauvin, The dam-break problem for concentrated suspensions of neutrally buoyant particles, J. Fluid Mech. 724 (2013) 95–122.
[20] K.M. Park, H.S. Yoon, M.I. Kim, CFD-DEM based numerical simulation of liquid-gas-particle mixture flow in dam break, Commun. Nonlinear Sci. Numer. Simul. 59 (2018) 105–121.
[21] P. Coussot, Structural similarity and transition from Newtonian to non-Newtonian behavior for clay-water suspensions, Phys. Rev. Lett. 74 (20) (1995) 3971.
[22] A.W. Saak, H.M. Jennings, S.P. Shah, A generalized approach for the determination of yield stress by slump and slump flow, Cem. Concr. Res. 34 (3) (2004) 363–371.
[23] N. Roussel, P. Coussot, "Fifty-cent rheometer" for yield stress measurements: from slump to spreading flow, J. Rheol. 49 (3) (2005) 705–718.
[24] J.-M. Piau, Consistometry slump and spreading tests: practical comments, J. Non-Newtonian Fluid Mech. 135 (2–3) (2006) 177–178.
[25] P. Perona, Bostwick degree and rheological properties: an up-to-date viewpoint, Appl. Rheol. 15 (EPFL-ARTICLE-149755) (2005) 218–229.
[26] R.R. Milczarek, K.L. McCarthy, Relationship between the bostwick measurement and fluid properties, J. Texture Stud. 37 (6) (2006) 640–654.
[27] N. Balmforth, R. Craster, P. Perona, A. Rust, R. Sassi, Viscoplastic dam breaks and the Bostwick consistometer, J. Non-Newtonian Fluid Mech. 142 (1–3) (2007) 63–78.
[28] E.B. Pitman, L. Le, A two-fluid model for avalanche and debris flows, Phil. Trans. R. Soc. London A 363 (1832) (2005) 1573–1601.
[29] C. Goniva, C. Kloss, A. Hager, S. Pirker, An open source CFD-DEM perspective, Proceedings of OpenFOAM Workshop, Göteborg 2010, pp. 1–10.
[30] J. Zhao, T. Shan, Numerical modeling of fluid-particle interaction in granular media, Theor. Appl. Mech. Lett. 3 (2) (2013), 021007. .
[31] J. Zhao, T. Shan, Coupled CFD-DEM simulation of fluid–particle interaction in geomechanics, Powder Technol. 239 (2013) 248–258.
[32] T. Shan, J. Zhao, A coupled CFD-DEM analysis of granular flow impacting on a water reservoir, Acta Mech. 225 (8) (2014) 2449–2470.
[33] J. Zhao, N. Guo, Rotational resistance and shear-induced anisotropy in granular media, Acta Mech. Solida Sin. 27 (1) (2014) 1–14.
[34] J. Zhao, N. Guo, The interplay between anisotropy and strain localisation in granular soils: a multiscale insight, Géotechnique 65 (8) (2015) 642–656.
[35] T. Zhao, G. Houlsby, S. Utili, Investigation of granular batch sedimentation via DEM-CFD coupling, Granul. Matter 16 (6) (2014) 921–932.
[36] T. Zhao, F. Dai, N. Xu, Coupled DEM-CFD investigation on the formation of landslide dams in narrow rivers, Landslides 14 (1) (2017) 189–201.
[37] L. Jing, C. Kwok, Y. Leung, Y. Sobral, Extended CFD–DEM for free-surface flow with multi-size granules, Int. J. Numer. Anal. Methods Geomech. 40 (1) (2016) 62–79.
[38] T.B. Anderson, R. Jackson, Fluid mechanical description of fluidized beds. Equations of motion, Ind. Eng. Chem. Fundam. 6 (4) (1967) 527–539.
[39] Y. Tsuji, T. Tanaka, T. Ishida, Lagrangian numerical simulation of plug flow of cohesionless particles in a horizontal pipe, Powder Technol. 71 (3) (1992) 239–250.
[40] Y. Tsuji, T. Kawaguchi, T. Tanaka, Discrete particle simulation of two-dimensional fluidized bed, Powder Technol. 77 (1) (1993) 79–87.
[41] H.G. Weller, G. Tabor, H. Jasak, C. Fureby, A tensorial approach to computational continuum mechanics using object-oriented techniques, Comput. Phys. 12 (6) (1998) 620–631.
[42] C. Kloss, C. Goniva, Liggghts: a new open source discrete element simulation software, Proceedings of The Fifth International Conference on Discrete Element Methods, London, UK 2010, pp. 25–26.
[43] P.A. Cundall, O.D. Strack, A discrete numerical model for granular assemblies, Géotechnique 29 (1) (1979) 47–65.
[44] Y. Zhou, B. Wright, R. Yang, B.H. Xu, A.B. Yu, Rolling friction in the dynamic simulation of sandpile formation, Physica A 269 (2–4) (1999) 536–553.
[45] J.F. Steffe, Rheological Methods in Food Process Engineering, Freeman press, 1996.
[46] A.A. Al-Habahbeh, Simulations of Newtonian and Non-Newtonian Flows in Deformable TubesPh.D. thesis Michigan Technological University, 2013.
[47] H. Zhu, Z. Zhou, R. Yang, A. Yu, Discrete particle simulation of particulate systems: theoretical developments, Chem. Eng. Sci. 62 (13) (2007) 3378–3396.
[48] C. O'Sullivan, Particulate Discrete Element Modelling: A Geomechanics Perspective, CRC Press, 2014.
[49] R. Di Felice, The voidage function for fluid-particle interaction systems, Int. J. Multiphase Flow 20 (1) (1994) 153–159.
[50] K. Kafui, C. Thornton, M. Adams, Discrete particle-continuum fluid modelling of gas–solid fluidised beds, Chem. Eng. Sci. 57 (13) (2002) 2395–2410.
[51] C. Goniva, C. Kloss, N.G. Deen, J.A. Kuipers, S. Pirker, Influence of rolling friction on single spout fluidized bed simulation, Particuology 10 (5) (2012) 582–591.
[52] E.M. Smuts, D.A. Deglon, C.J. Meyer, Methodology for CFD-DEM modelling of particulate suspension rheology, Proceedings of the Ninth International Conference on CFD in the Minerals and Process Industries CSIRO, Melbourne, Australia, 2012.
[53] M. Bagherzadeh, Modelling Single Particle Settlement by CFD-DEM Coupling MethodPh.D. thesis Delft University of Technology, 2014.
[54] Z. Zhou, S. Kuang, K. Chu, A. Yu, Discrete particle simulation of particle–fluid flow: model formulations and their applicability, J. Fluid Mech. 661 (2010) 482–510.
[55] C. Biscarini, S. Di Francesco, P. Manciola, CFD modelling approach for dam break flow studies, Hydrol. Earth Syst. Sci. 14 (4) (2010) 705.
[56] G. Lube, H.E. Huppert, R.S.J. Sparks, A. Freundt, Static and flowing regions in granular collapses down channels, Phys. Fluids 19 (4) (2007), 043301. .
[57] E. Lajeunesse, J. Monnier, G. Homsy, Granular slumping on a horizontal surface, Phys. Fluids 17 (10) (2005), 103302. .
[58] H.E. Huppert, The propagation of two-dimensional and axisymmetric viscous gravity currents over a rigid horizontal surface, J. Fluid Mech. 121 (1982) 43–58.
[59] J.-M. Piau, K. Debiane, Consistometers rheometry of power-law viscous fluids, J. Non-Newtonian Fluid Mech. 127 (2–3) (2005) 213–224.
[60] F. Yazdandoost, J. Attari, Hydraulics of Dam and River Structures, Taylor & Francis, 2004.
[61] H. Chanson, Hydraulics of open channel flow, Butterworth-Heinemann, 2004.
[62] H. Rouse, Critical analysis of open-channel resistance, J. Hydraul. Div. 91 (4) (1965) 1–23.
[63] B.C. Yen, Open channel flow resistance, J. Hydraul. Eng. 128 (1) (2002) 20–39.
[64] G.E. Grant, Critical flow constrains flow hydraulics in mobile-bed streams: a new hypothesis, Water Resour. Res. 33 (2) (1997) 349–358.
[65] O. Pouliquen, Y. Forterre, Friction law for dense granular flows: application to the motion of a mass down a rough inclined plane, J. Fluid Mech. 453 (2002) 133–151.
[66] A. Armanini, M. Larcher, M. Odorizzi, et al., Dynamic impact of a debris flow front against a vertical wall, Proceedings of the 5th International Conference on Debris-Flow Hazards Mitigation: Mechanics, Prediction and Assessment, Padua, Italy 2011, pp. 1041–1049.
[67] S.B. Savage, K. Hutter, The motion of a finite mass of granular material down a rough incline, J. Fluid Mech. 199 (1989) 177–215.
[68] R.M. Iverson, The physics of debris flows, Rev. Geophys. 35 (3) (1997) 245–296.